JCI The Journal of Clinical Investigation

An *in vivo* screening platform identifies senolytic compounds that target *p16^{INK4a+}* fibroblasts in lung fibrosis

Jin Young Lee, … , Michelle R. Arkin, Tien Peng

J Clin Invest. 2024. https://doi.org/10.1172/JCI173371.

Research In-Press Preview Aging Pulmonology

Graphical abstract

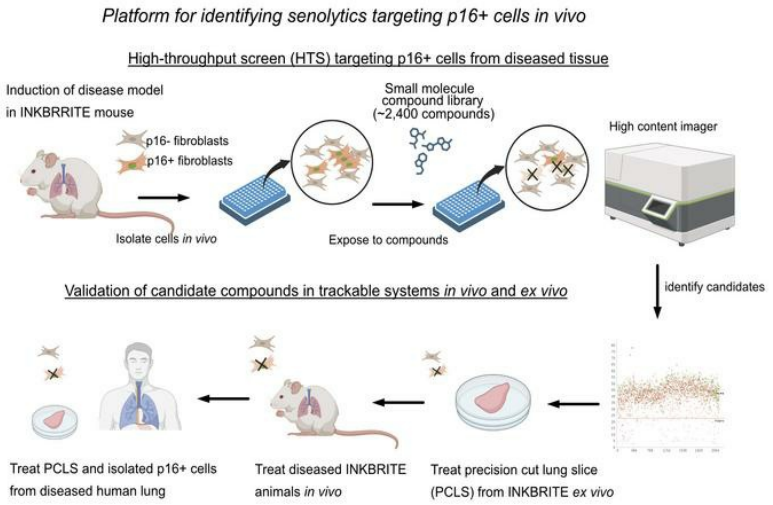

Title

An *in vivo* screening platform identifies senolytic compounds that target *p16^{INK4a}*+ fibroblasts in lung fibrosis

Authors

Jin Young Lee[1], Nabora S. Reyes[1], Supriya Ravishankar[1], Minqi Zhou[1], Maria Krasilnikov[1], Christian Ringler[1], Grace Pohan[2], Chris Wilson[2], Kenny Kean-Hooi Ang[2], Paul J. Wolters[1], Tatsuya Tsukui[1], Dean Sheppard[1], Michelle R. Arkin[2] and Tien Peng[1,3*]

[1]Department of Medicine, Division of Pulmonary, Critical Care, Allergy, and Sleep
[2]Small Molecule Discovery Center
[3]Bakar Aging Research Institute
University of California San Francisco
San Francisco, CA, USA

*Address correspondence to:
Tien Peng, M.D.
University of California, San Francisco
513 Parnassus Ave.
HSE Building, Room 1312, Box 0130
San Francisco, CA 94143
Phone: 415.514.4180
Email: tien.peng@ucsf.edu

Conflict of interest statement:

The authors have declared that no conflict of interest exists.

Abstract

The appearance of senescent cells in age-related diseases has spurred the search for compounds that can target senescent cells in tissues (“senolytics”). However, a major caveat with current senolytic screens is the use of cell lines as targets where senescence is induced *in vitro*, which does not necessarily reflect the identity and function of pathogenic senescent cells *in vivo*. Here, we developed a new pipeline leveraging a fluorescent murine reporter that allows for isolation and quantification of *p16^{Ink4a}*+ cells in diseased tissues. By high-throughput screening *in vitro*, precision cut lung slice (PCLS) screening *ex vivo*, and phenotypic screening *in vivo*, we identified a HSP90 inhibitor (XL888) as a potent senolytic in tissue fibrosis. XL888 treatment eliminated pathogenic *p16^{Ink4a}*+ fibroblasts in a murine model of lung fibrosis and reduced fibrotic burden. Finally, XL888 preferentially targeted *p16^{INK4a}*-high human lung fibroblasts isolated from patients with idiopathic pulmonary fibrosis (IPF), and reduced *p16^{INK4a}*+ fibroblasts from IPF PCLS *ex vivo*. This study provides proof of concept for a platform where *p16^{INK4a}*+ cells are directly isolated from diseased tissues to identify compounds with *in vivo* and *ex vivo* efficacy in mouse and human respectively and provides a senolytic screening platform for other age-related diseases.

Introduction

Hayflick's original description of a stereotyped proliferative arrest for primary cells in culture as "senescence at the cellular level (1)" gave way to geroscience that seeks to unravel the relationship between cellular aging and age-related diseases (2). While initial studies of senescence mostly occurred in cell culture, the identification of biomarkers *in vitro* was extrapolated to study *in vivo* phenomena in aging tissues, exemplified by the use of *p16^{INK4a}* expression as a biomarker of senescent cells in tissues (3). The construction of mouse models where *p16^{Ink4a}*+ cells can be genetically depleted to ameliorate a host of age-related phenotypes validated this approach (4-9), and identified senescent cells in tissues as potential targets for pharmacotherapy (10). The pipeline to identify compounds targeting senescent cells ("senolytics") involves screening cytotoxicity on cell lines where senescence is induced *in vitro*, followed by validation in preclinical animal models where senescent cells are thought to be present (11). However, this approach assumes that senescent cells derived from cell lines in culture are identical to senescent cells *in vivo* that reside in far more diverse cellular environments.

Single cell transcriptome analyses have demonstrated that senescent phenotypes *in vitro* are heterogeneous and dependent on senescence inducers and cell types (12, 13). Based on these studies, senescent cells *in vivo* would be expected to display even more functional heterogeneity given the diverse tissue microenvironment they would encounter. Leveraging an ultrasensitive GFP reporter of *p16^{Ink4a}* (Ink4a-H2B-GFP reporter-in-tandem, or INKBRITE), we recently demonstrated that *p16^{Ink4a}*+ fibroblasts *in vivo* exhibit a spectrum of senescent phenotypes that directly correlated

with the range of *p16*^{Ink4a} transcript levels (14). The recognition that senescent cells are functionally heterogeneous has profound implications for senolytic screening pipelines, as target cell type selection could significantly influence the candidates identified. This has already become apparent as different senolytic screens have identified compounds that have non-overlapping efficacy against different cell types and preclinical models (15). To improve the ability to identify senolytics with *in vivo* efficacy against the disease of interest, we set out to develop a screening platform that 1) utilizes senescent cells directly isolated from diseased tissues as screening targets, and 2) provides an *in vivo* platform for direct validation of senolytic activity in the tissue of origin.

Idiopathic pulmonary fibrosis (IPF) is an age-related lung disease where telomere shortening and senescence have been implicated in the pathogenesis (16, 17). Histologic examination of IPF lungs have demonstrated the presence of biomarkers associated with senescence in alveolar type 2 (AT2) cells and lung fibroblasts (18), which was confirmed in single cell atlases of IPF lungs showing enrichment of *CDKN2A* (encoding *p16*^{INK4a}) expression in epithelial and fibroblast subsets (19, 20). Despite histologic evidence of p16^{INK4a}+ cells in IPF and animal models of lung fibrosis, their pathogenic role is less clear. Genetic ablation of *p16*^{Ink4a}+ cells in an animal model of lung fibrosis improved lung function, but there was no evidence that this animal model improved standard fibrotic endpoints such as hydroxyproline content (21). Furthermore, genetic depletion studies preclude the ability to identify *p16*^{Ink4a}+ cells in the fibrotic tissue and study their behavior in a prospective manner. To determine whether *p16*^{Ink4a}+ cells are a viable target for therapeutic intervention in lung fibrosis, we need to isolate and characterize these cells *in vivo*. In this study, we characterized the identity of

fibrotic *p16*^{Ink4a}+ fibroblasts *in vivo* and outlined a senolytic screening platform that provides scalability and validation by leveraging the ability to isolate and track *p16*^{Ink4a}+ cells from diseased tissues. Utilizing our new platform, we identified a novel senolytic compound that deleted *p16*^{Ink4a}+ cells and reduced fibrotic burden in a murine model of lung fibrosis, and preferentially targeted *p16*^{INK4a}+ fibroblasts from human IPF lung samples.

Results

Murine *p16^{Ink4a}*+ lung fibroblasts display profibrotic identities and phenotypes *in vivo*.

Our previous study showed that *p16^{Ink4a}*+ fibroblasts dynamically respond to tissue injury in the lung (14). To define the potential contribution of *p16^{Ink4a}*+ fibroblasts to fibrogenesis, we performed single cell RNAseq (scRNAseq) on fibrotic INKBRITE lungs. Leveraging our capacity to isolate *p16^{Ink4a}*+ cells by fluorescent sorting, we isolated GFP+ fibroblasts (CD45- EpCAM- CD31-) from lungs of INKBRITE mice treated with bleomycin (14 days post injury, or dpi). We profiled 7,846 cells and identified 6 clusters with distinct marker gene expressions that corresponded with previously annotated fibroblast subsets identified in fibrotic murine lungs (22, 23) (Figure 1A, Supplemental Figure 1, A and B). In addition to the adventitial, alveolar, and peribronchial fibroblast subsets that were previously identified in the uninjured lungs, we observed significant fractions of “pathologic” (expressing numerous pro-fibrotic genes) and stress-activated fibroblasts that were found to arise *de novo* in the fibrotic lung (Figure 1, A-C) (22, 23). These pathologic fibroblasts were mostly absent from our prior single cell dataset of *p16^{Ink4a}*+ fibroblasts isolated from naphthalene injured INKBRITE lungs (14) (Supplemental Figure 1, A-E), showing that the lineage fate of *p16^{Ink4a}*+ fibroblasts changes with the injury context. Immunohistochemistry (IHC) of injured INKBRITE lungs demonstrated infiltration of GFP+ fibroblasts within dense, fibrotic regions (Figure 1D, dashed circles). IHC analysis validated the scRNAseq results, demonstrating the presence of *p16^{Ink4a}*+/*Cthrc1*+ fibroblasts within the fibrotic regions that also contain other fibrotic markers such as ACTA2, COL1A1, and TAGLN (Figure 1D).

To determine phenotypic differences between *p16*^{Ink4a}- and *p16*^{Ink4a}+ fibroblasts in fibrotic tissue, we FACSorted GFP+ and GFP- fibroblasts from bleomycin-injured INKBRITE lungs for downstream analyses. Quantitative PCR (pPCR) confirmed the upregulation of *p16*^{Ink4a} as well as p21 in GFP+ fibroblasts, along with phenotypic markers associated with senescence such as cell size, DNA damage, and proliferative arrest (Supplemental Figure 2, A-E). Furthermore, *p16*^{Ink4a}+ fibroblasts demonstrated significant upregulation for genes enriched in pathologic fibroblasts compared to *p16*^{Ink4a}- fibroblasts (Figure 1E), which was confirmed on immunocytochemistry of sorted GFP+ and GFP- fibroblasts from fibrotic INKBRITE lungs (Supplemental Figure 3, A-C). To investigate potential differences in response to fibrotic stimuli between *p16*^{Ink4a}+ and *p16*^{Ink4a}- cells, we isolated GFP+ and GFP- lung fibroblasts from uninjured INKBRITE lungs and stimulated them with recombinant TGF-β1. *p16*^{Ink4a}+ fibroblasts exhibit elevated fibrotic gene expression both before and after TGF-β1 stimulation compared to *p16*^{Ink4a}- fibroblasts (Figure 1F). These data indicate that *p16*^{Ink4a}+ lung fibroblasts preferentially give rise to pathologic fibroblasts in lung fibrosis. More importantly, our data suggest that different types of *p16*^{Ink4a}+ fibroblasts arise in different pathologic contexts, which could also dictate divergent susceptibility of *p16*^{Ink4a}+ cells to senolytics under different tissue conditions.

_p16_^{Ink4a} expression in lung fibroblasts augments the fibrotic response.

To determine the role of *p16*^{INK4a} expression in the fibrotic response, we first generated a dual lentiviral system (Lenti-tTS/rtTA + Lenti-TRE-p16-T2A-dTomato) to overexpress *p16*^{INK4a} in a doxycycline-dependent manner (14). Primary human lung fibroblasts

isolated from control cadaveric donors were transduced with our *p16^{INK4a}* overexpression (OE) vectors, followed by doxycyline and fibrotic induction *in vitro* (addition of TGF-β1). *p16^{INK4a}* OE significantly augmented the expression of pathologic fibroblast genes in response to TGF-β1 compared to control fibroblasts (Figure 2A). Interestingly, *p16^{INK4a}* OE in the absence of TGF-β1 did not induce pro-fibrotic gene expression (Figure 2A), suggesting the *p16^{INK4a}* alone does not independently drive the fibrotic response, but rather primes the fibroblast response to a fibrotic stimulus.

To determine the necessity of *p16^{Ink4a}* expression in the fibroblast response to fibrotic stimuli *in vivo*, we deleted *p16^{Ink4a}* in fibroblasts with a mesenchymal-specific Cre-driver (*Dermo1$^{Cre/+}$*). As we had previously reported, fibroblast-specific deletion of *p16^{Ink4a}* (*Dermo1$^{Cre/+}$:p16$^{flox/flox}$*, referred to as *D1^{p16CKO}*) did not alter the gross morphology in the uninjured lung(14). Induction of fibrotic injury with bleomycin demonstrated that *D1^{p16CKO}* animals exhibited attenuated fibrotic response on histology and collagen deposition (as measured by hydroxyproline) compared to controls (Figure 2, B and C). IHC analysis demonstrated that fibroblast-specific deletion of *p16^{Ink4a}* reduced the number of fibroblasts expressing pro-fibrotic markers in the bleomycin-injured lungs (Figure 2, D and E). These experiments demonstrated that *p16^{Ink4a}* expression primes the fibroblasts to augment the fibrotic response but is not sufficient to drive fibrosis in the absence of a fibrotic stimulus.

High throughput screen (HTS) identified compounds targeting *p16^{Ink4a}*+ lung fibroblasts isolated from fibrotic tissue.

Proper target selection is one of the most important factors for successful compound screens. To identify compounds that will specifically target *p16*^{Ink4a}+ fibroblasts from fibrotic lungs, we leveraged the ability to isolate *p16*^{Ink4a}+ fibroblasts *in vivo* from diseased tissues utilizing the INKBRITE reporter. We purified *p16*^{Ink4a}+ (GFP+) and *p16*^{Ink4a}- (GFP-) fibroblasts *in vivo* directly from the fibrotic lungs of INKBRITE animals injured with bleomycin (14 dpi). The fluorescent tag allowed us to mix GFP+ and GFP- fibroblasts at a 1:1 ratio into 384-well plates, so that each well can serve as an internal control when comparing the cell viability of *p16*^{Ink4a}+ and *p16*^{Ink4a}- fibroblasts. The ability to combine the target (*p16*^{Ink4a}+) and bystander (*p16*^{Ink4a}-) cells together in the same well also allowed us to scale up the screen to a chemical library of roughly 2,000 small molecules with annotated biologic activity (Figure 3A). The goal of the primary screen was to identify the most potent compounds that killed off GFP+ fibroblasts while sparing GFP- fibroblasts as determined by the percentage of GFP+ fibroblasts (%GFP+) in each well. The fluorescent intensity of the INKBRITE reporter and nuclear localization of H2B-GFP allowed image segmentation of GFP+ and GFP- nuclei in over 2,600 wells with high content imaging, and we identified 37 compounds that exceeded the statistical threshold of 3 sigma (<20%GFP+) from the mean (45%GFP+ in negative control/vehicle wells) (Figure 3, B and C). Analysis of the annotated biological pathways demonstrated numerous pathways previously implicated in senolysis (24) (*eg.* HSP90, BCL-2, PI3K inhibitors) as well as potentially novel ones (eg. HDAC, proteasome inhibitor) (Figure 3D). Of note, previously identified senolytics such as dasatinib, quercetin, and fisetin all reduced %GFP+ below the mean, but none exceeded the 3-sigma threshold for secondary validation (Supplemental Table 1).

To define the potency of these compounds to delete *p16*^{Ink4a}+ cells, we selected 32 compounds with the lowest %GFP+ for secondary validation with dose-response curves to determine the half-maximal inhibitory concentration (IC50) for reduction of %GFP+ fibroblasts (Figure 3E). Each compound was tested over 10 concentrations to a maximum of 20 mM. The validation screen yielded 8 compounds that had an IC50 (%GFP) below 2 uM, which was composed mostly of HSP90 and HDAC inhibitors (Supplemental Table 2). The top candidates typically had a maximal effect (E_{max}) of reducing GFP+ fibroblast viability <10% (Supplemental Figure 4). The top 3 candidates had IC50 (reduction of %GFP) below 1 uM, and they were Trichostatin A (TSA, HDAC inhibitor), XL888 (heat shock protein 90, or HSP90 inhibitor), and Ganetesipib (HSP90 inhibitor) (Figure 3F).

An *ex vivo* model using precision cut lung slices (PCLS) to validate senolytic candidates.

A bottleneck to the compound screening pipeline is narrowing the top hits that are most likely to be efficacious in animal disease models, which can be expensive and time-consuming to perform. To predict *in vivo* efficacy to streamline our screen, we incorporated an *ex vivo* platform to test the top hits in our screen in a more physiologic setting that is easily scalable. *Ex vivo* culture of precision cut lung slices (PCLS) has been utilized to model lung diseases such as IPF as well as drug testing for lung fibrosis (25). We first generated PCLS cultures from bleomycin-injured INKBRITE animals (Figure 4, A and B). Flow cytometry analysis demonstrated high viability of the cells in the PCLS at the end of the 5-day culture period (Supplemental Figure 5A). We tested

the top candidates identified in the secondary validation in the fibrotic INKBRITE PCLS *ex vivo* using the same standard drug concentration as the primary screen. Again, we wanted to examine the effect of the compound on *p16*^{Ink4a}+ fibroblasts relative to *p16*^{Ink4a}- fibroblasts, so we examined the %GFP in the fibroblast population (CD45-/EpCAM-/CD31-, Figure 4C) on flow analysis of the treated PCLS. Flow analysis demonstrated that both HSP90 inhibitors (XL888 and ganetespib) reduced the %GFP+ fibroblasts in the INKBRITE PCLS, while TSA had no effect (Figure 4D and Supplemental Figure 5B). Histology of INKBRITE PCLS demonstrated preserved architecture and continued presence of ACTA2+/*p16*^{Ink4a}+ and COL1+/*p16*^{Ink4a}+ fibroblasts in the fibrotic regions of the lung (Figure 4E). IHC analysis of XL888-treated PCLS demonstrated a reduction of GFP+ACTA2+ and GFP+COL1+ fibroblasts (Figure 4, E and F). We also screened two other HDAC inhibitors with low IC50 in the dose-response validation *in vitro* (fimepinostat and dacinostat), but neither compound reduced %GFP+ fibroblasts *ex vivo* in our PCLS assay (Supplemental Figure 5C). Finally, we tested other previously described senolytics in our PCLS model (dasatinib+quercetin or D&Q, fisetin, ABT-263 and ABT-737) in comparison with XL888, and only XL888 reduced %GFP+ fibroblasts compared to vehicles (Supplemental Figure 5D). GFP over-expression in normal lung fibroblasts did not enhance susceptibility to XL888-mediated killing (Supplemental Figure 5E). Finally, we tested XL888 on PCLS isolated from INKBRITE animals induced with a non-fibrotic injury using naphthalene (airway injury followed by full repair). In contrast to fibrotic injured PCLS, XL888 did not significantly reduce the % of GFP+ fibroblasts from naphthalene injured PCLS (Supplemental Figure 5F). These experiments suggest that HSP90

inhibitors are the most promising candidates to target *p16*^{Ink4a}+ fibroblasts *in vivo* in preclinical animal models of lung fibrosis.

XL888 deletes *p16*^{INK4a}+ lung fibroblasts *in vivo* and attenuates fibrotic remodeling in mice.

To determine whether the PCLS screen correlated with *in vivo* activity against *p16*^{Ink4a}+ fibroblasts, we set up an *in vivo* validation step where each of the candidate compounds tested in PCLS (XL888, ganetespib, TSA, fimepinostat, and dacinostat) was administered in our preclinical model of lung fibrosis and compared against vehicle-treated control animals (each compound required a different vehicle cohort because each is formulated differently with different routes of administration). INKBRITE animals were first injured with bleomycin to establish fibrosis, followed by administration of the candidate senolytic daily for 2 weeks (Figure 5A). For each compound, we determined the maximum effective dose based on literature search of previous use in other pre-clinical models. At the end of the treatment period, we determined the selective impact of the compound on *p16*^{Ink4a}+ fibroblasts using an identical flow cytometry strategy as described for PCLS (Figure 4C). Flow analysis of single cell lung suspension at the end of the study period demonstrated that only XL888 treatment resulted in a significant reduction in the %GFP+ fibroblasts *in vivo* compared to vehicle controls (Figure 5, B and C, Supplemental Figure 6, A-D).

To determine whether XL888 targeted pathologic *p16*^{Ink4a}+ subsets described in our scRNAseq analysis, we repeated the XL888 treatment in fibrotic INKBRITE animals for histologic analysis. IHC showed that treatment of XL888 reduced the GFP+/ACTA2+

fibroblasts within fibrotic regions of the lung (Figure 5, D and E). To determine whether XL888 reduced the overall fibrotic burden in the lung, we performed trichrome staining and hydroxyproline quantification in another cohort of XL888 treated animals compared with vehicles, which showed reduction in fibrotic remodeling in the lung as well as collagen content as measured by hydroxyproline (Figure 5, F and G). Finally, we administered D&Q in our preclinical model using the same dosing schedule as previously reported (21) (3 times for 3 weeks treatment period) in the INKBRITE mice, and we could not observe a difference in the %GFP+ fibroblasts at the end of the study period, although there was a trend towards reduction in %GFP+ immune and endothelial cells (Supplemental Figure 6, E-G). D&Q did not change the total collagen content by hydroxyproline assay (Supplemental Figure 6H). These results showed that XL888, identified from our HTS platform, effectively eliminated *p16*^{Ink4a}+ fibroblasts *in vivo* and attenuated pulmonary fibrosis in animal model. The results demonstrated that *p16*^{Ink4a}+ fibroblasts play a functional role in the development of lung fibrosis and indicate their potential as therapeutic targets for diseases involved in the accumulation of those cells.

Human *p16*^{INK4a}+ fibroblasts contribute to pathologic fibroblast subsets in IPF. While IPF fibroblasts cultured *in vitro* have been reported to demonstrate senescent characteristics (26), we sought to determine the expression pattern of *CDKN2A* (encoding both *p16*^{INK4a} and *p19*^{ARF}) in our previous scRNAseq of IPF lung fibroblasts i*n vivo* (22) (Figure 6A, Supplemental Figure 7A). Our previous analysis of IPF fibroblasts demonstrated distinct clusters of alveolar and adventitial fibroblasts comparable to

those defined in mice, along with the emergence of a *CTHRC1*+/*COL1A1*^{hi}/*ACTA2*^{hi} pathologic fibroblast subset similar to the one that arose in murine lungs after bleomycin injury (22). Analysis of *CDKN2A* expression showed significant enrichment in the *CTHRC1*+/*COL1A1*^{hi}/*ACTA2*^{hi} fibroblast subset that had been found to form fibroblastic foci in the IPF lungs (Figure 6, B-D). qPCR of IPF fibroblasts demonstrated significantly higher *p16*^{INK4a} expression compared to lung fibroblasts isolated from normal controls (Supplemental Figure 7B, patient demographics data in Supplemental Table 3). IHC analysis of IPF lungs demonstrated the presence of p16^{INK4a}+/ACTA2+ and p16^{INK4a}+/*CTHRC1*+ cells within areas of dense fibrotic remodeling, and the absence of these cells in the normal control lungs (Figure 6E, Supplemental Figure 7C).

We previously reported a technique to isolate senescent *p16*^{INK4a}-hi fibroblasts from the human lung by pulsing human lung fibroblasts with CellTrace Far Red (CT^{FR}), a fluorescent dye that is diluted with cell division, and isolating CT^{FR}-retaining (CT^{FR}-hi) cells that developed proliferative arrest in culture (14). We applied this technique to segregate CT^{FR}-hi and lo fibroblasts from IPF lungs (from patients undergoing lung transplantation), and qPCR demonstrated significant enrichment of *p16*^{INK4a} expression in the CT^{FR}-hi population (but not *p14*^{ARF} encoded in the same locus) along with other pathologic fibroblast markers such as *p21*, *CTHRC1*, *HAS1*, and *POSTN* (Figure 6F, Supplemental Figure 7D). These results demonstrate that profibrotic IPF lung fibroblasts are enriched for *p16*^{INK4a} expression, and they can be isolated for drug testing.

XL888 deletes human p16^{INK4a}+ fibroblasts from IPF lungs.

To determine whether XL888 preferentially targets *p16*^{INK4a}-hi relative to *p16*^{INK4a}-lo fibroblasts from human lungs, we sorted CT^{FR}-hi and lo fibroblasts isolated from explanted IPF lungs. CT^{FR}-hi and lo fibroblasts were sorted into separate wells and dose-escalation challenge with XL888 was performed along with other previously identified senolytics (ABT263, ABT737, and dasatinib) to determine their potency in deleting *p16*^{INK4a}-hi vs. *p16*^{INK4a} lo fibroblasts. Treatment of XL888 preferentially deleted CT^{FR}-hi fibroblasts compared to CT^{FR}-lo IPF fibroblasts (Figure 7A). In contrast, previously described senolytic compounds did not exhibit selective targeting of CT^{FR}-hi fibroblasts, similar to what we found in the PCLS derived from INKBRITE murine lungs (Supplemental Figure 5D). To investigate the potential efficacy of XL888 in IPF *ex vivo*, we utilized PCLS generated from IPF lung tissues (Figure 7B). Flow cytometry analysis indicated high viability of the cells in the PCLS at the end of the 5-day culture period (Supplemental Figure 7E). IHC analysis of human PCLS showed that XL888 treatment decreased pathologic p16^{INK4a}+ACTA2+ and p16^{INK4a}+CTHRC1+ fibroblasts (Figure 7, C and D). Taken together, these results demonstrate that our senolytic HTS identified a compound that preferentially targets *p16*^{INK4a}+ fibroblasts from fibrotic lungs, which was subsequently validated *in vivo* and *ex vivo* respectively in mouse models of lung fibrosis and human IPF samples.

Discussion

The success of high-throughput screens (HTS) of small molecules, as defined by the identification of compounds that are effective *in vivo*, is highly dependent on whether the screening target approximates the physiological target that will ultimately serve to validate the discovery (27). Molecular and cellular targets are selected based on their relevance to the disease state, as well as the ease with which these targets can be obtained. Over the past decade, remarkable progress has been made on the identification of “senolytics,” or compounds targeting cells with senescent properties that have been implicated in age-related pathologies. Hypothesis-driven candidate screens that identified senolytics such as D&Q, navitoclax, and fisetin have been shown to display *in vivo* efficacy in disease models (10, 28, 29), however, the cellular targets for these senolytics are not redundant. Utilizing various human cell lines where senescence is induced *in vitro*, these early studies showed that different senolytics have cell-type specific efficacy *in vitro*, which accounts for the difference in their efficacy in different mouse disease models *in vivo*. This suggested a heterogeneity in the mechanisms adopted by senescent cells to resist apoptosis and highlighted the need for a more rational approach where the screening target cell type directly approximates the pathogenic cell type *in vivo* being targeted. An ideal screening platform would utilize disease and organ-specific senescent cells as the screening target, coupled with a reporter system to validate whether the drug candidates are targeting the same cell type *in vivo*. However, a major challenge in the field has been isolating senescent cells *in vivo* for prospective studies, as early mouse reporters of senescence (based on the

expression of *p16*^{Ink4a}) have been mostly utilized to delete senescent cells for functional studies.

We recently generated an ultrasensitive fluorescent reporter of *p16*^{Ink4a} (INKBRITE) that allowed us to identify cells with senescent characteristics *in vivo* as well as to isolate them from tissues (14). Utilizing this tool, we wanted to determine whether we could improve the existing senolytic screening pipeline by increasing the precision and scalability of HTS. We chose lung fibrosis as our model disease because *p16*^{Ink4a}+ cells have been previously reported to arise *de novo* in the fibrotic lung (19, 20, 26, 30), but the therapeutic role for existing senolytics is less clear. Utilizing our INKBRITE model, we identified specific *p16*^{INK4a}+ cell types present in the fibrotic lungs of mouse and human, showing the contribution of senescent cells to a pathologic fibroblast subtype that was recently implicated in driving fibrotic remodeling (22, 23). More importantly, our single cell analysis demonstrated that the fate of *p16*^{Ink4a}+ fibroblasts is context dependent, as we did not observe the emergence of pathologic *p16*^{Ink4a}+ fibroblasts in a different injury model (naphthalene) with a different regenerative outcome. This supports the emerging view that senescent cells are not monolithic, but rather represent heterogeneous subpopulations that are capable of diverse responses to physiologic stimuli that can be harmful or beneficial (31). This is highlighted by our data that *p16*^{INK4a} expression alone is not sufficient to drive the fibrotic response, but rather serves to prime the fibroblasts for maximal fibrotic induction in response to TGF-β1.

The context dependent nature of *p16*^{Ink4a}+ fibroblasts would also suggest that their susceptibility to cell killing could differ across tissue states *in vivo*, thus providing

the rationale for a senolytic platform that targets specific pathologic contexts. By using *p16^{Ink4a}*+ fibroblasts isolated from fibrotic lungs as the screening target while simultaneously using *p16^{Ink4a}*- fibroblasts as the control within the same well, we were able to scale up the HTS to include over 2,000 compounds with known biologic activity. Furthermore, the ability to track these cells allowed us to utilize fibrotic INKBRITE lungs to validate the efficacy of candidate senolytics in deleting *p16^{Ink4a}*+ fibroblasts in preclinical models. This pipeline can be easily retrofitted to identify candidate senolytics in alternative disease models where *p16^{Ink4a}*+ cells play a pathogenic role. As part of our screening pipeline, we also leveraged the PCLS *ex vivo* culture system to validate our HTS and streamline our discovery platform. Our study highlights the potential utility of the PCLS for preliminary drug screening prior to *in vivo* experimentation, given its capacity to maintain fibrotic fibroblasts in their native tissue architecture and preserved extracellular environment comparable to intact tissues (32). We showed high concordance in the efficacy of candidate senolytic in deleting *p16^{Ink4a}*+ cells when comparing PCLS *ex vivo* with whole animal *in vivo*. This approach can significantly streamline the screen and reduce the amount of animal testing, which is the most costly and time-consuming part of the pipeline. Furthermore, it allows us to extend our studies into human diseased tissues in parallel with preclinical animal models to strengthen the target validation process (Supplemental Figure 8).

Our screening platform ultimately identified XL888, an HSP90 inhibitor, as the most promising senolytic in our screen for lung fibrosis. XL888 was one of the top hits in the initial HTS, and we were able to validate its potency in deleting *p16^{Ink4a}*+ fibroblasts in both preclinical model of murine lung fibrosis as well as PCLS of IPF lung tissue.

Importantly, XL888 attenuated multiple fibrotic indicators, including total collagen content, in the preclinical model of lung fibrosis. XL888 is currently in Phase I clinical trials as a potential anti-cancer agent in solid tumors (33), but our study would suggest a potential role in fibrotic diseases. While our screen was hypothesis-free, it was reassuring that we identified a compound class that has previously been shown to exhibit senolytic properties. HSP90 inhibitors such as geldamycin and 17-AAG were identified in a previous screen targeting progeroid fibroblasts in mice (29), although neither compound achieved our 3-sigmal threshold for secondary validation.

Together, our findings demonstrated that senescent cells, as identified by our novel INKBRITE reporter for *p16^{Ink4a}*, contribute to profibrotic fibroblasts in pulmonary fibrosis. Furthermore, leveraging HTS with our *in vivo* reporter, we identified a new senolytic compound and validated its efficacy in fibrosis through direct measurement of senescent cell reduction *in vivo* along with attenuation of disease phenotype. We also described a method to isolate *p16^{INK4a}*+ cells from human tissues to validate candidate senolytics in patient samples that will strengthen the rationale for clinical trials. A major caveat of our study is that clearly not all *p16^{INK4a}*+ cells are functionally senescent. Our prior work had shown that senescent characteristics correlated with *p16^{INK4a}* expression in the lung fibroblasts *in vivo*, which represented a spectrum of phenotypes rather than a digital (on and off) property (14). This illustrates the complexity of senescent phenotypes *in vivo* that is not as well described compared to senescent cells *in vitro*, but also supports the necessity of screening against cellular targets *in vivo* to increase our understanding of how senolytics function to target specific subtypes of cells with senescent properties arising *in vivo*.

Methods

Human lung samples

Studies involving human tissue were approved by the UCSF Institutional Review Board. All subjects provided written informed consent. Peripheral regions of the normal lungs were obtained to select for the distal regions of the lung from brain-dead donors that were rejected for lung transplantation. IPF lung specimens were taken from the periphery of the lung at the time of lung transplant. Age and sex of tissue donors are listed in Supplementary Table 3.

Sex as a biological variable

Sex was not considered as a biological variable.

Animal studies

All mice were housed and treated in accordance with the IACUC protocol approved at the University of California, San Francisco. Mice between the ages of 8-12 weeks old were used for the experiments with balance of gender between groups. C57BL/6 mice were obtained from Jackson Laboratory. Generation and genotyping of INKBRITE and *Dermo1*$^{Cre/+}$*:p16*$^{flox/flox}$ lines were performed as previously described (14). For bleomycin-induced injury, mice were given pharmaceutical-grade bleomycin (Hospira) dissolved in PBS via intranasal instillation (2.5 U per kg body weight). For naphthalene injury, mice were administered with 300 mg/kg of naphthalene (Sigma) dissolved in corn oil by intraperitoneal injection. For XL888 treatment, mice were treated with 62.5 mg/kg via oral delivery 5 days a week for 2 weeks starting 10 days after bleomycin injury. XL888 was dissolved in 10 mM hydrochloric acid (HCL) with the concentration of 15.625

mg/ml. After vigorous vortexing, the dissolved XL888 was delivered to the mice using oral gavage daily. For DQ treatment in mice, C57BL/6 mice received a single dose of bleomycin (2.5 U/kg, day 1) and received dasatinib (5 mg/kg) and quercetin (50 mg/kg) at day 5, 11, and 17 following the previous study (21). Whole lung tissues from the mice were collected at day 23 for hydroxyproline assay.

Histology and immunohistochemistry

For paraffin embedded mouse lungs, mouse right ventricles were perfused with 1 ml PBS and the lungs were inflated with 4% PFA, and then fixed in 4% PFA overnight at 4°C. After fixation, the lungs were washed by cold PBS X 4 times in 2 hrs at 4°C and dehydrated in a series of increasing ethanol concentration washes (30%, 50%, 70%, 95% and 100%). The dehydrated lungs were incubated with Xylene for 1 hr at RT and with paraffin at 65°C for 90 min X 2 times, and then embedded in paraffin and sectioned. Human and mouse PCLS samples were fixed in 4% PFA for 30 mins. After PBS washes, slices were embedded in OCT after 30% sucrose incubations. 6-8 μm thick cryosections were used for immunohistochemistry. Following antibodies were used: GFP (1:400, Abcam, ab6673), Alpha smooth muscle actin (1:200, Abcam, ab5694), Transgelin (1:200, Abcam, ab14106), and Collagen I (1:200, Abcam, ab21286). Human lung fragments were fixed and processed as the mouse lungs. Antibodies used for human lung slide staining were ACTA2 (1:200, Abcam, ab5694), $p16^{INK4a}$ (1:200, Santa Cruz, sc-56330), and CTHRC1 (1:200, Abcam, ab85739). Collagen staining was performed using Trichrome stain kit according to the

manufacturer's protocol (Abcam, ab150686). Images were captured using Zeiss Imager M1 or Leica Stellaris 5.

RNA *in situ*

Paraffin-embedded lung sections were used for RNA in situ detection of Cthrc1 using a RNAscope Multiplex Fluorescent Reagent kit (ACD biotechne) according to the manufacturer's instructions.

Lung digestion and Fluorescence Activated Cell Sorting (FACS)

Dissected mouse lung was tracheally perfused with a digestion cocktail of Collagenase Type I (225 U/ml, Thermo Fisher), Dispase (15 U/ml, Thermo Fisher) and Dnase (50 U/ml, Sigma) after perfusion with PBS and removed from the chest. The lung was incubated in a digestion cocktail for 45 mins at 37°C with continuous shaking. The mixture was then washed with a FACS buffer (2% FBS and 1% Penicillin-Streptomycin in DMEM). The mixture was passed through a 70 μm cell strainer and resuspended in a red blood cell (RBC) lysis buffer, then passed through a 40 μm cell strainer. Cell suspensions were incubated with the appropriate conjugated antibodies in a sorting buffer for 30 min at 4°C and washed with FACS buffer. Doublets and dead cells were excluded based on forward and side scatter and SYTOX Blue (Invitrogen, S34857), respectively.

The following antibodies were used for staining: CD45-PE-Cy7 (Invitrogen, 50-112-9643), CD45-BV421 (BD, 563890), CD31-BV711 (BD, 740680), CD31-BV421 (Invitrogen, 48-0311-82), EpCAM-PE (BD, 563477), EpCAM-BV421 (BD, 563214).

Immune (CD45-biotin, Biolgened, 103104), epithelial (CD326-biotin, Biolegend, 118204) and endothelial (CD31-Biotin, Biolegend, 102404) cells are removed with EasySep mouse streptavidin RapidShperes (StemCell, 19860A), when applicable. FACS was performed on a BD FACS Aria using FACSDiva Software. CD45- CD31- EpCAM- cells were sorted for mesenchymal cells, the GFP- and GFP+ fibroblasts were further separated and were sorted into FACS buffer. Analysis was performed using FlowJo software.

For the human lung, a distal piece (~10 cm^3) was dissected from the whole lung and washed with HBSS X 4 times in 15 min. The piece of lung was further diced with razor blades and was added into the digestion cocktail of Collagenase Type I (225 U/ml, Thermo Fisher), Dispase (15 U/ml, Thermo Fisher) and Dnase (100 U/ml, Sigma). The mixture was incubated for 2 h at 37°C and vortexed intermittently. The mixture was then liquefied with a blender and passed through 4X4 gauze, a 100 mm and a 70 mm cell strainer. The mixture was resuspended in RBC lysis buffer, before passing through a 40 mm cell strainer. The cell suspensions were incubated with the antibodies in the FACS buffer for 30 min at 4°C and washed with the FACS buffer. The following antibodies were used for staining: CD45-APC-Cy7 (BioLegend, 304014), CD31-APC-Cy7 (BioLegend, 303120), CD11b-APC-Cy7 (BD Biosciences, 557754), EpCAM-PE (BioLegend, 324206). DAPI (0.2 mg/ml) was used to exclude dead cells. Single cells were selected and CD45- CD11b- CD31- EpCAM- cells were sorted for mesenchymal cells. Cells were sorted into FACS buffer. FACS analysis was performed by FACSDiva (BD).

Quantitative RT-PCR (qPCR)

Total RNA was obtained from cells using PicoPure RNA Isolation Kit (Applied Biosystems, KIT0204) or RNeasy mini kit (QIAGEN, 74106), following the manufacturers' protocols. cDNA was synthesized from total RNA using the SuperScript Strand Synthesis System (Thermo Fisher, 18080044). Quantitative RT-PCR (qRT-PCR) was performed using the SYBR Green system (Thermo Fisher, F415L). Relative gene expression levels after qRT-PCR were defined using the ΔΔCt method and normalizing to the housekeeping genes. The qRT-PCR primers used for mouse are as follows: Cthrc1-F: CAGTTGTCCGCACCGATCA; Cthrc1-R: GGTCCTTGTAGACACATTCCATT; Col1a1-F; TGACTGGAAGAGCGGAGAGT; Col1a1-R:GTTCGGGCTGATGTACCAGT; Col3a1-F: CTGTAACATGGAAACTGGGGAAA; Col3a1-R: CCATAGCTGAACTGAAAACCACC; Spp1-F: AGCAAGAAACTCTTCCAAGCAA; Spp1-R: GTGAGATTCGTCAGATTCATCCG; Acta2-F: ACTCTCTTCCAGCCATCTTTCA; Acta2-R: ATAGGTGGTTTCGTGGATGC; Postn-F: TGGTATCAAGGTGCTATCTGCG; Postn-R: AATGCCCAGCGTGCCATAA; S100a4-F: TGAGCAACTTGGACAGCAACA; S100a4-R: CTTCTTCCGGGGCTCCTTATC; Tagln-F: GGTGGCTCAATTCTTGAAGGC; Tagln-R: TGCTCCTGGGCTTTCTTCATA; p16INK4a-F: AATCTCCGCGAGGAAAGC; p16INK4a-R: GTCTGCAGCGGACTCCAT; p21-F: TAAGGACGTCCCACTTTGCC; p21-R: CGTCTCCGTGACGAAGTCAA; Gapdh-F: GGCCCCTCCTGTTATTATGGGGGT; Gapdh-R: CCCCAGCAAGGACACTGAGCAAGA. The primers used for human are as follows: *p16INK4a*-F: GTCGGGTAGAGGAGGTGCG; *p16INK4a*-R: CATGACCTGGATCGGCCTC; *p21*-F: TTGTACCCTTGTGCCTCGCT; *p21*-R:

CGTTTGGAGTGGTAGAAATCTGTC; *CTHRC1*-F: GTGGCTCACTTCGGCTAAAAT; *CTHRC1*-R: CACTAATCCAGCACCAATTCCTT; *HAS1*-F: TCAAGGCGCTCGGAGATTC; *HAS1*-R: CTACCCAGTATCGCAGGCT; *SPP1*-F: GAAGTTTCGCAGACCTGACAT; *SPP1*-R: GTATGCACCATTCAACTCCTCG; *POSTN*-F: CTCATAGTCGTATCAGGGGTCG; *POSTN*-R: ACACAGTCGTTTTCTGTCCAC; *ACTA2*-F: AAAAGACAGCTACGTGGGTGA; *ACTA2*-R: GCCATGTTCTATCGGGTACTTC; *COL1A1*-F: GGGGTAAGTCCCTTTCTGCC; *COL1A1*-R: ATTGCCTTTGATTGCTGGGC; *RPL19*-F: CCCATCTTTGATGAGCTTCC; *RPL19*-R: TGCTCAGGCTTCAGAAGAGG.

Single-cell RNA sequencing and analysis

Single cell sequencing was performed on a 10X Chromium instrument (10X Genomics) at the Institute of Human Genetics (UCSF, San Francisco, CA). Briefly, live mouse lung cells were sorted and resuspended in 50 µl PBS with 0.04% BSA at 1,000 cells/µl and loaded onto a single lane into the Chromium Controller to produce gel bead-in emulsions (GEMs). GEMs underwent reverse transcription for RNA barcoding and cDNA amplification. The library was prepped with the Chromium Single Cell 3' Reagent Version 3 kit. The samples were sequenced using the HiSeq2500 (Illumina) in Rapid Run Mode. We used the Seurat R package along with a gene-barcode matrix provided by CellRanger for downstream analysis. Following the standard workflow of Seurat, we generated Seurat objects after using ScaleData, RunPCA, RunUMAP. For human scRNA-seq data, we used processed scRNA-seq data from normal and IPF lungs from

GSE147066. After generating subsets of lung fibroblasts, violin plots and density plots were generated.

Cell Culture

Freshly isolated mesenchymal cells from INKBRITE lungs (GFP- or GFP+) or human lung fibroblasts were cultured in DMEM/F-12 (Thermo Fisher, 11330032) with 10% FBS and 1% Pen/Strep. The medium was changed every 2 days and lung fibroblasts were maintained for no more than 3 passages.

TGF-β1 *in vitro* stimulation

Fibroblasts were sorted from fibrotic INKBRITE lungs. $1x10^5$ cells were seeded into 48 well plates and cultured in DMEM/F12 with 2% FBS and 1% Pen/Strep for 24 h. Medium was changed to serum free DMEM with 1% Pen/Strep for 24 h. After the serum starvation, medium was changed to serum-free DMEM/F-12 with 1% Pen/Strep and 1 ng/ml TGF-β1 (Peprotech, 10778-032). After 24-48 h stimulation, RNA was obtained using RNeasy mini kit (QIAGEN, 74106).

Lentivirus infection

Primary human lung fibroblasts were seeded and infected the following day with lentivirus (Lenti- tTS/rtTA, Lenti-TRE-p16INK4a-T2A-dTomato). On day 1, the fibroblasts were infected with lentivirus at 5 multiplicity of infection (MOI) in DMEM-F12 with 10% FBS and polybrene at 5 µg/ml. On day 2, cells were washed with 1X PBS 4 times and placed on regular media (DMEM-F12, 10%FBS, 1% PS). Doxycycline (1 µg/ml)

treatment began 72 to 96 hours later for Lenti-tTS/rtTA and Lenti-TRE-p16 dual-transduced cells.

Adenovirus infection

Primary mouse lung fibroblasts were seeded and infected the following day with adenovirus expressing GFP. On day 1, the fibroblasts were infected with adenovirus at 260 MOI in DMEM-F12 with 10% FBS. On day 2, cells were washed with 1X PBS 4 times and placed on regular media (DMEM-F12, 10%FBS, 1% PS). Cells were treated with XL888 from day 3 to day 6.

High-throughput screening

The screen was performed in collaboration with the Small Molecule Discovery Center (SMDC) at UCSF. INKBRITE mice received a single dose of bleomycin at 2.5 U/kg and lung tissues were collected 14 days after the injury. Single cell suspension of the lung was prepared and sorted as described above. A suspension of GFP+ and GFP- fibroblast cells (1:1 ratio) was plated in 384 well-plates (Greiner Bio-One, 781096) at 2000 cells/well density using WellMate^{TM} liquid dispenser (Matrix). After an overnight incubation, 2400 test compounds from SelleckChem bioactive and epigenetic library were added using Biomek FXp (Beckman Coulter) pin tools to a final concentration of 1 µM, followed by a 3-day incubation. On the third day, plates were washed with 1X PBS and NucView530 dye mix was dispensed at 2 µM final concentration into each well using EL406 washer dispenser (BioTek), followed by an hour incubation. Plates were then washed with 1X PBS and fixed with an addition of 4% PFA + 1µg/ml Hoechst mix

into each well. After 15 min incubation, plates were washed with 1X PBS and imaged. Fluorescence images were captured using IN Cell Analyzer 6500HS (Cytiva) at 20X magnification, 4 field-of-views per well. Images were processed using IN Cell Developer Tool Box. Nuclear mask was created from the Hoechst channel and was applied to both GFP and NucView channels to calculate the number of total cells, GFP+, GFP-, and NucView+ cells.

Compounds that caused GFP+ cell count to be below the 3SD limit of the negative control (wells with no test compound) were determined as hit candidates. Thirty-two compounds were selected for a follow up validation screen based on compounds' identity and targets. Dose response curves and their IC50s were generated for these 32 compounds with the concentration ranging between 0.005 μM to 2.5 μM (2-fold dilution).

Generation of precision-cut lung slices (PCLS) culture

For mouse PCLS, INKBRITE mice were injured with 2.5 U/kg of bleomycin and lung tissues were collected 2 weeks after the injury. The lungs were perfused with PBS through the right ventricle and inflated with 1 to 2 ml of 2% agarose (Thermo Fisher, 16550100) dissolved in PBS by trachea. After inflation, the trachea was tied with a suture to prevent agarose leakage. Lungs were dissected from the chest cavity and submerged in ice-cold PBS to solidify agarose. Lung lobes were sliced at a width of 500 μm using a vibratome (Leica, VT 1000S).

For human PCLS, fresh lung tissues were obtained from IPF patients that underwent lung transplantation. After washing with PBS, the tissues were inflated with

warm 2% agarose and placed in cold PBS. The lung specimens were cut into strips and sliced into 600 μm thick slices using a vibratome.

The slices were cultured in DMEM/F-12 (Thermo Fisher, 11330032) with 1% Pen/Strep under standard cell culture conditions (37C, 5% CO2). ABT263 (2.5 μM), ABT737 (2 μM), Fisetin (10 μM), DQ (1 μM + 20 μM), and XL888 (1 μM) were treated during the culture. 1 μM of concentration was used for other candidate compounds (TSA, ganetespib, fimepinostat, and dacinostat). At day 5, cultured PCLSs were processed for downstream analyses.

Flow cytometry analysis of mouse PCLS

The lung slices were placed into 15 ml conical tubes containing 1 ml of digestion cocktail of Dispase (3 U/ml, Thermo Fisher) and Dnase (50 U/ml, Sigma) after PBS washes. The slices were incubated in a digestion cocktail for 30 mins at 37°C with continuous shaking. The mixture was then washed with a FACS buffer (2% FBS and 1% Penicillin-Streptomycin in DMEM). The mixture was passed through a 70 μm cell strainer. Cells were stained with antibodies and analyzed by flow cytometry as described above.

Hydroxyproline assay

Collagen content in the lungs was assessed by measuring the hydroxyproline level using the Hydroxyproline Colorimetric Assay Kit (K555-100) from BioVision. Briefly, lung tissue was homogenized in water and the homogenized samples were hydrolyzed by incubation with 12N hydrochloric acid at 120°C for 3 hours. The hydrolysates were

oxidized using chloramine T, followed by incubation with Ehrlich's perchloric acid reagent. Absorbance was measured at 560 nm.

CellTrace Far Red (CT^{FR})

Isolated fibroblasts were cultured for 3 days and stained with CellTrace Far Red reagent. The fibroblasts were detached and stained with 1 μM of CellTrace for 20 minutes at 37°C (1 million cells per ml) following the manufacturer's protocol. After staining, the cells were washed with media and cultured for 3 to 4 days. Serum-starved cells after CT^{FR} staining were used to separate CT^{FR} high and low cells based on CT^{FR} levels. CT^{FR} stained cells within the high intensity range of 95 to 97% encompassing serum-starved, non-proliferating cells were sorted as CT^{FR} high cells, while cells exhibiting a lower intensity range were sorted as CT^{FR} low cells.

Statistics

All data are presented as mean ± SD. Statistical differences between the groups were compared using unpaired two-tailed Student's *t* test or one-tailed Student's *t* test for 2 groups or 1-way ANOVA for multiple groups. Statistical significance was defined as $*P < 0.05$, $**P < 0.01$, $***P < 0.001$. Statistical details and the number of replicates for each experiment can be found in the figure legends. The following formula is used to compute sample size and power:

$$n_A = \kappa n_B \text{ and } n_B = \left(1 + \frac{1}{\kappa}\right)\left(\sigma \frac{z_{1-\alpha/2} + z_{1-\beta}}{\mu_A - \mu_B}\right)^2$$

$$1 - \beta = \Phi\left(z - z_{1-\alpha/2}\right) + \Phi\left(-z - z_{1-\alpha/2}\right) \quad , \quad z = \frac{\mu_A - \mu_B}{\sigma\sqrt{\frac{1}{n_A} + \frac{1}{n_B}}}$$

κ=nA/nBκ=nA/nB is the matching ratio
σ is standard deviation
Φ is the standard normal distribution function
Φ−1 is the standard normal quantile function
α is Type I error
β is Type II error, meaning 1−β is power

Study approval

Animal husbandry and all experiments were conducted under Institutional Animal Care and Use Committee-approved protocols at University of California, San Francisco (No. AN191522-01J). Human specimen isolation from explanted lungs of patient undergoing lung transplantation at UCSF is approved by Institutional Review Board at UCSF (No. 13-10738).

Data availability

Previously published human scRNA-seq data that are re-analyzed in this study are available in NCBI Gene Expression Omnibus (GEO) under the accession number GSE147066. The sequencing data of the mouse that support the findings of this study have been deposited in the accession number GSE235352. The values for all data points in graphs are reported in the Supporting Data Values file.

Author contributions

J.L. and T.P. conceived the experiments and wrote the manuscript. J.L., S.R., M.Z., M.K., N.R., C.R., G.P., C.W., K.A., and T.T. performed the experiments. P.W. provided clinical specimen. D.S. and M.A. provided expertise and feedback.

Acknowledgements

We thank Parnassus Flow Cytometry Core for assistance with cell sorting for bulk and single cell RNA analysis (P30DK063720). GEO accession number for raw RNA sequencing data is listed in Methods. This work is supported by NIH grants R01HL160895 and R01HL155622 and CIRM DISC0-14460 to T.P., the Tobacco-Related Disease Research Program (TRDRP) postdoctoral award T33FT6395 and Basic Science Research Program through the National Research Foundation of Korea (NRF) funded by the Ministry of Education (2020R1A6A3A03038781) to J.L., and Nina Ireland Program Award for human lung collection.

Figure Legends

Figure 1. *p16^{Ink4a}*+ fibroblasts contribute to pathologic fibroblasts in mouse model of lung fibrosis.

(**A**) Experimental scheme for scRNAseq of *p16^{Ink4a}*+ (GFP+) fibroblasts from the INKBRITE lung after bleomycin-induced fibrosis (14 dpi).

(**B**) Violin plot showing profibrotic gene expressions in the different *p16^{Ink4a}*+ fibroblast subsets *in vivo*.

(**C**) Visualization of *Acta2*, *Cthrc1*, *Col1a1* and *Tagln* expression pattern within the fibroblast subsets.

(**D**) Representative images showing *Cthrc1* (RNAscope in situ), ACTA2, TAGLN, and COL1A1 (immunostaining) in lung sections of bleomycin-injured INKBRITE mice (14 dpi) co-localized with GFP (arrows: *p16^{Ink4a}*+ fibroblasts). Scale bars, 100 μm.

(**E**) qPCR analysis of purified GFP+ and GFP- fibroblasts from bleomycin-treated INKBRITE lungs (n = 5-6 biological replicates, experiment repeated 2X).

(**F**) qPCR analysis of cultured GFP+ and GFP- fibroblasts isolated from fibrotic INKBRITE lungs after treatment of recombinant TGF-β1 or vehicle (n =3 technical replicates, experiment repeated 2X).

Data are represented as mean ± SD.; **P* < 0.05; ***P* < 0.01; ****P* < 0.001; two-tailed Student's t test (**E**); or one-way ANOVA (**F**).

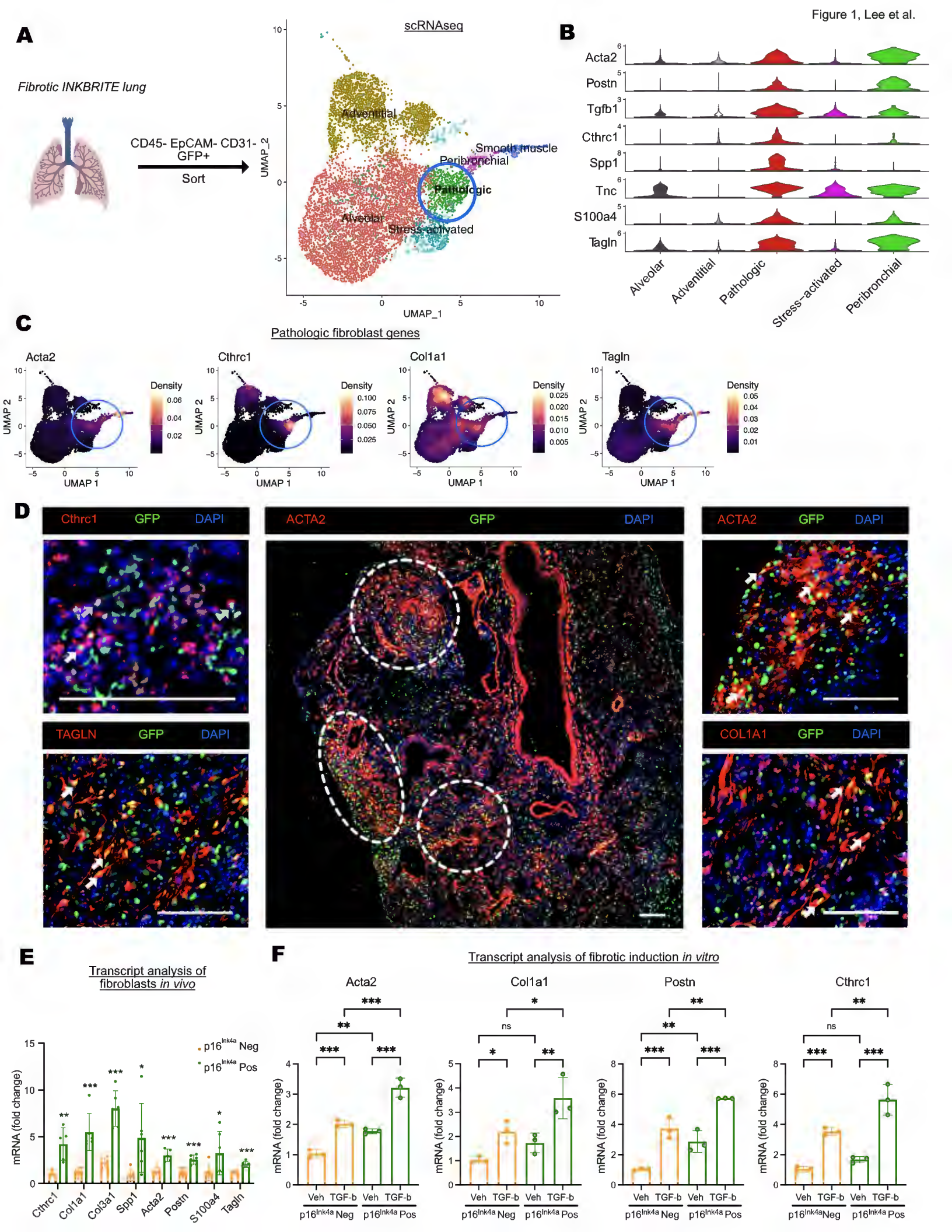
A
Fibrotic INKBRITE lung
CD45- EpCAM- CD31- GFP+
Sort
scRNAseq
Adventitial
Smooth muscle
Peribronchial
Pathologic
Alveolar
Stress-activated
UMAP_1
UMAP_2
B
Acta2
Postn
Tgfb1
Cthrc1
Spp1
Tnc
S100a4
Tagln
Alveolar
Adventitial
Pathologic
Stress-activated
Peribronchial
C
Pathologic fibroblast genes
Acta2
Cthrc1
Col1a1
Tagln
Density
UMAP 1
UMAP 2
D
Cthrc1 GFP DAPI
ACTA2 GFP DAPI
TAGLN GFP DAPI
COL1A1 GFP DAPI
E
Transcript analysis of fibroblasts in vivo
p16Ink4a Neg
p16Ink4a Pos
mRNA (fold change)
Cthrc1
Col1a1
Col3a1
Spp1
Acta2
Postn
S100a4
Tagln
F
Transcript analysis of fibrotic induction in vitro
Acta2
Col1a1
Postn
Cthrc1
mRNA (fold change)
Veh
TGF-b
p16Ink4a Neg
p16Ink4a Pos
ns

Figure 2. *p16^{INK4a}* expression primes lung fibroblasts to augment the fibrotic response.

(**A**) Transcript analysis of cultured primary human lung fibroblast isolated from control cadaveric donors transduced with two lentiviral vectors to overexpress (OE) human *p16^{INK4a}* with doxycycline induction followed by addition of TGF-β1. (n =3 technical replicates, experiment repeated 2X)

(**B**) Representative H&E sections of *Dermo1$^{Cre/+}$;p16$^{flox/flox}$* and control (*p16$^{flox/flox}$*) animals injured with bleomycin to induce lung fibrosis.

(**C**) Hydroxyproline assay to quantify collagen in the left lung of *Dermo1$^{Cre/+}$;p16$^{flox/flox}$* and control animals 14 days following bleomycin injury (n = 5 control, 9 mutant biological replicates).

(**D**) Representative IHC showing ACTA2 and COL1 immunostaining in lung sections of bleomycin-injured *Dermo1$^{Cre/+}$;p16$^{flox/flox}$* and control (*p16$^{flox/flox}$*) animals (14 dpi).

(**E**) IHC quantification of ACTA2+ and COL1+ fibroblasts from (D) (n = 5 control, 9 mutant biological replicates), Scale bars, 200 μm.

Data are represented as mean ± SD.; **P* < 0.05; ***P* < 0.01; ****P* < 0.001; two-tailed Student's t test (**A**, **C**, **E**).

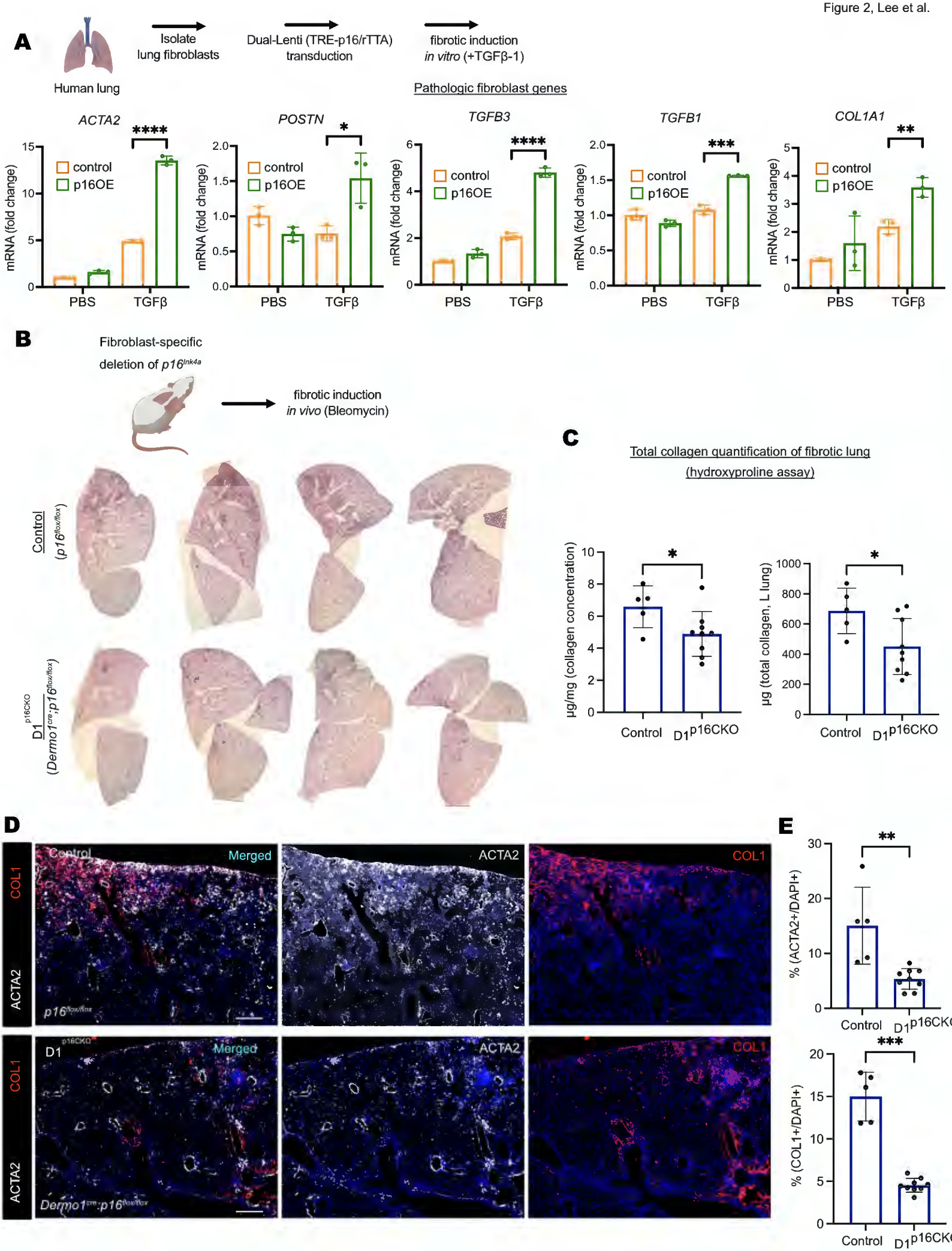
A
Human lung
Isolate lung fibroblasts
Dual-Lenti (TRE-p16/rTTA) transduction
fibrotic induction in vitro (+TGFβ-1)
Pathologic fibroblast genes
ACTA2
POSTN
TGFB3
TGFB1
COL1A1
mRNA (fold change)
control
p16OE
PBS
TGFβ
B
Fibroblast-specific deletion of p16Ink4a
fibrotic induction in vivo (Bleomycin)
Control (p16flox/flox)
D1p16CKO (Dermo1cre:p16flox/flox)
C
Total collagen quantification of fibrotic lung (hydroxyproline assay)
μg/mg (collagen concentration)
μg (total collagen, L lung)
Control
D1p16CKO
D
COL1
ACTA2
Merged
E
% (ACTA2+/DAPI+)
% (COL1+/DAPI+)

Figure 3. High-throughput screen (HTS) targeting *p16^{Ink4a}*+ fibroblasts isolated from fibrotic INKBRITE lungs.

(**A**) Schematic outline of the HTS to identify compounds targeting *p16^{Ink4a}*+ (GFP+) fibroblasts from the fibrotic INKBRITE lungs.

(**B**) Scatter plot showing hit results from each well containing compound (pink) or vehicle (green). Y-axis indicate %GFP+ cells in each well after compound exposure. Compounds exceeding 3-sigma for lowest %GFP were selected for validation.

(**C**) Cell count GFP+ and GFP- fibroblasts of the top senolytic candidates.

(**D**) Biologic pathways targeted by the top senolytic candidates.

(**E**) Schematic outline of dose-response analysis of the top senolytic candidate from the primary screen.

(**F**) Top candidates emerging from the secondary validation using dose-response with lowest IC50 values, including trichostatin A, XL888, and ganetespib.

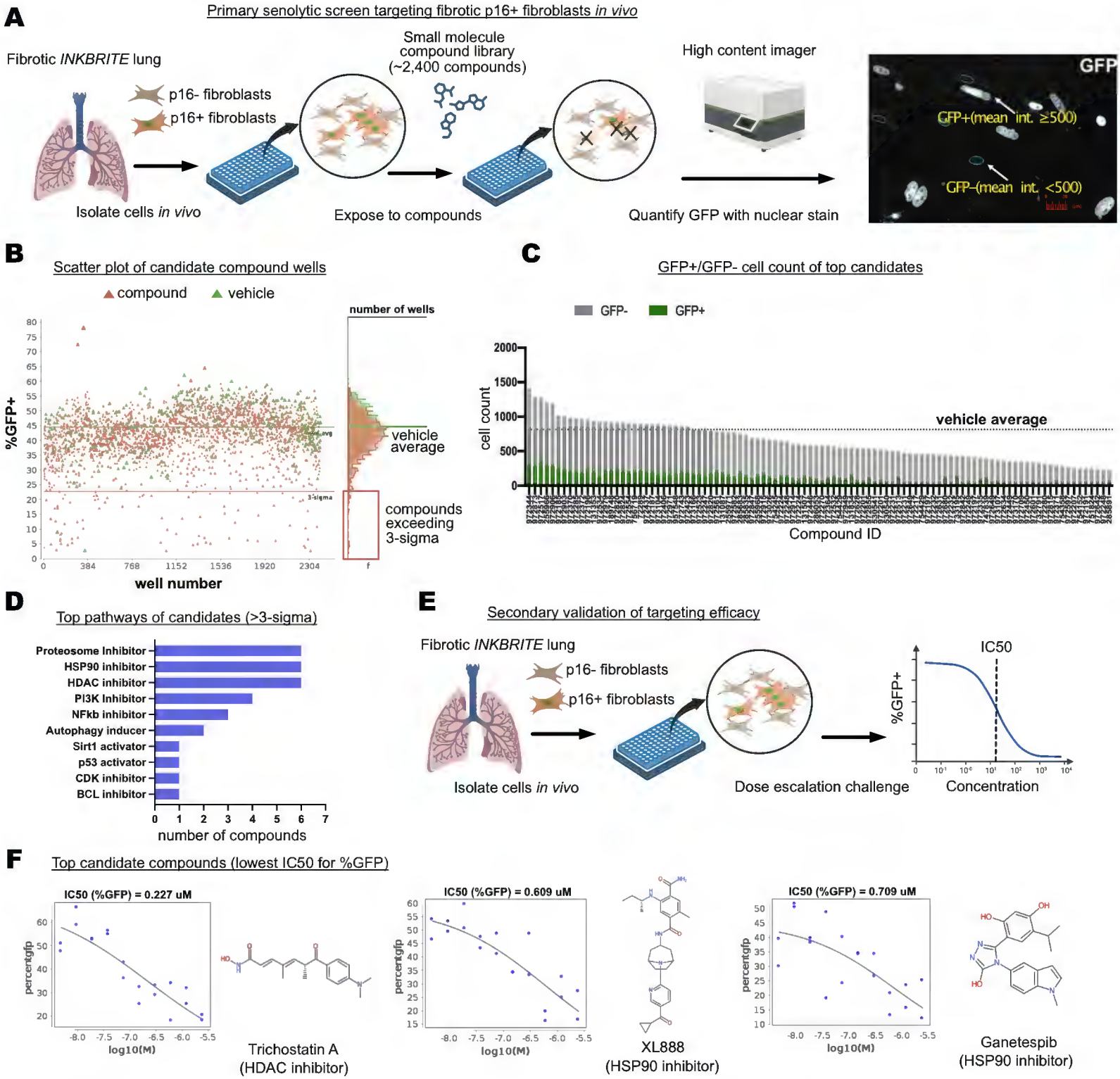
A
Primary senolytic screen targeting fibrotic p16+ fibroblasts *in vivo*
Fibrotic *INKBRITE* lung
p16- fibroblasts
p16+ fibroblasts
Isolate cells *in vivo*
Small molecule compound library (~2,400 compounds)
Expose to compounds
High content imager
Quantify GFP with nuclear stain
GFP
GFP+(mean int. ≥500)
GFP-(mean int. <500)
B
Scatter plot of candidate compound wells
compound
vehicle
%GFP+
well number
number of wells
vehicle average
compounds exceeding 3-sigma
C
GFP+/GFP- cell count of top candidates
GFP-
GFP+
cell count
vehicle average
Compound ID
D
Top pathways of candidates (>3-sigma)
Proteosome Inhibitor
HSP90 inhibitor
HDAC inhibitor
PI3K Inhibitor
NFkb inhibitor
Autophagy inducer
Sirt1 activator
p53 activator
CDK inhibitor
BCL inhibitor
number of compounds
E
Secondary validation of targeting efficacy
Fibrotic *INKBRITE* lung
p16- fibroblasts
p16+ fibroblasts
Isolate cells *in vivo*
Dose escalation challenge
IC50
%GFP+
Concentration
F
Top candidate compounds (lowest IC50 for %GFP)
IC50 (%GFP) = 0.227 uM
percentgfp
log10(M)
Trichostatin A
(HDAC inhibitor)
IC50 (%GFP) = 0.609 uM
XL888
(HSP90 inhibitor)
IC50 (%GFP) = 0.709 uM
Ganetespib
(HSP90 inhibitor)

Figure 4. Validation of candidate senolytic compounds using mouse precision-cut lung slices (PCLS) derived from fibrotic INKBRITE lungs.

(**A**) Experimental scheme for *ex vivo* culture of mouse PCLS derived from fibrotic INKBRITE mouse to test senolytic candidates.

(**B**) Bright field and GFP images of cultured PCLS. Scale bars= 2000 μm.

(**C**) Gating strategy to analyze GFP+ fibroblasts from mouse PCLS by flow cytometry.

(**D**) Quantification of GFP+ fibroblasts in the PCLS cultured with vehicle or XL888 (1 μM) for 5 days (n=10 technical replicates, experiment repeated 2X).

(**E**-**F**) Immunofluorescence analysis (**E**) and quantification (**F**) of ACTA2, COL1A1, and GFP in mouse PCLS treated with vehicle or XL888 (1 μM). (n=9 technical replicates, experiment repeated 2X). Scale bars, 50 μm.

Data are represented as mean ± SD.; **P* < 0.05; ***P* < 0.01; ****P* < 0.001; two-tailed Student's t test (**D**, **F**).

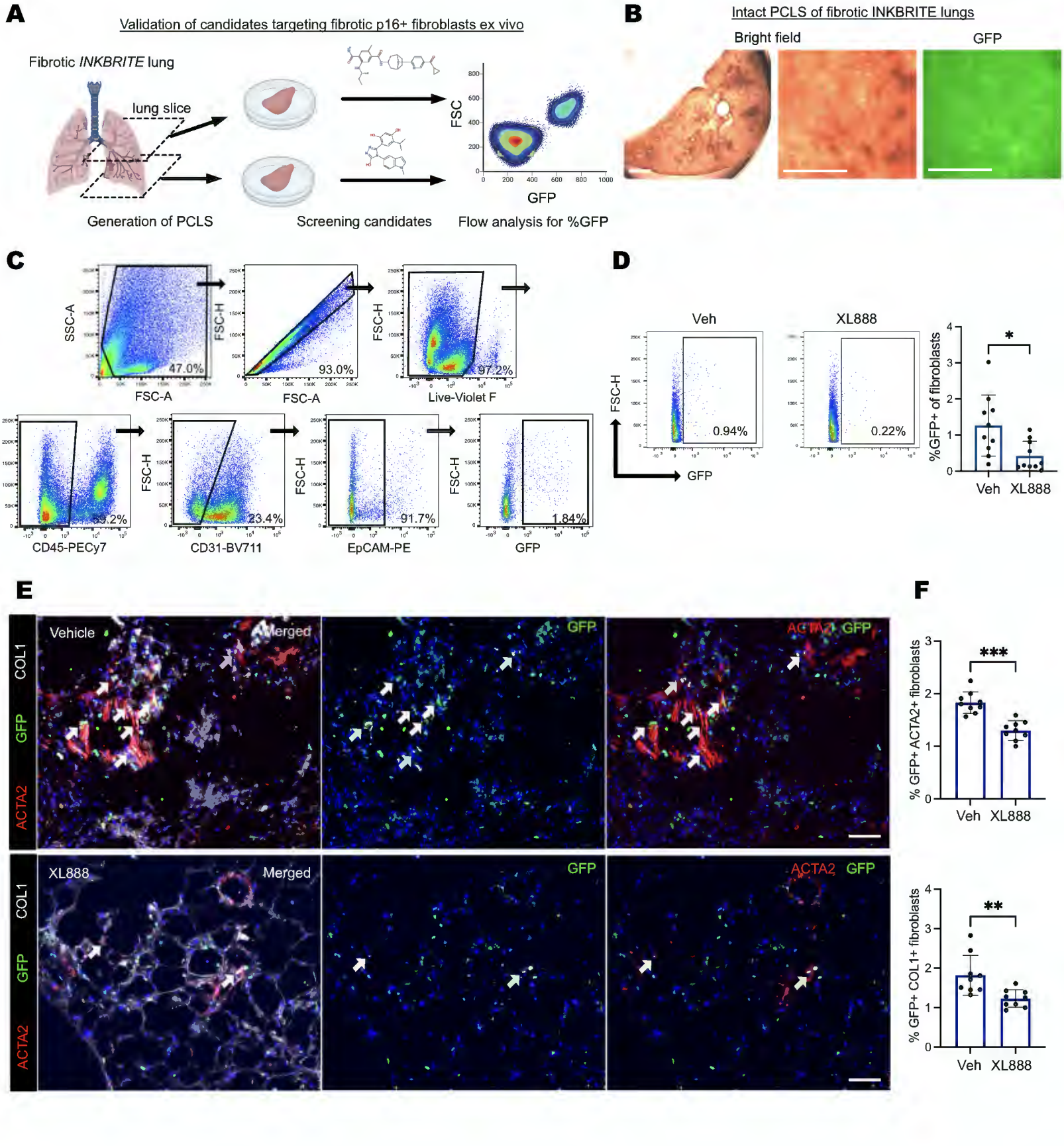
A
Validation of candidates targeting fibrotic p16+ fibroblasts ex vivo
Fibrotic INKBRITE lung
lung slice
Generation of PCLS
Screening candidates
FSC
GFP
Flow analysis for %GFP
B
Intact PCLS of fibrotic INKBRITE lungs
Bright field
GFP
C
SSC-A
FSC-A
47.0%
FSC-H
93.0%
Live-Violet F
97.2%
CD45-PECy7
69.2%
CD31-BV711
23.4%
EpCAM-PE
91.7%
GFP
1.84%
D
Veh
XL888
FSC-H
0.94%
0.22%
GFP
%GFP+ of fibroblasts
Veh
XL888
E
Vehicle
Merged
COL1
GFP
ACTA2
XL888
F
% GFP+ ACTA2+ fibroblasts
% GFP+ COL1+ fibroblasts

Figure 5. XL888 deletes *p16^{Ink4a}*+ fibroblasts and attenuates fibrotic remodeling *in vivo.*

(**A**) Schematic outline of animal experiments to validate *in vivo* efficacy of candidate senolytics.
(**B**-**C**) Flow cytometry analysis of GFP+ fibroblasts (% of fibroblasts that are GFP+) in bleomycin-injured lungs of vehicle or XL888 delivered INKBRITE animals (n = 11-12 biological replicates, experiment repeated 2X).
(**D**-**E**) Immunofluorescence analysis (**D**) and quantification (**E**) of GFP+ cells among ACTA2+ fibroblasts in the lungs of vehicle or XL888-treated INKBRITE mice (n = 4 biological replicates, experiment repeated 2X). Scale bars, 100 μm.
(**F**) Representative images (left) and quantification of Masson's trichrome staining of lung sections from indicated group of mice after bleomycin injury (n = 4 biological replicates). Scale bars, 1000 μm.
(**G**) Quantitative analysis of collagen in lung homogenates from vehicle or XL888 treated animals injured with bleomycin (n = 19-20 biological replicates, experiment repeated 2X).
Data are represented as mean ± SD.; **P* < 0.05; ***P* < 0.01; ****P* < 0.001; two-tailed Student's t test (**C**); or one-tailed Student's t test (**E**-**G**).

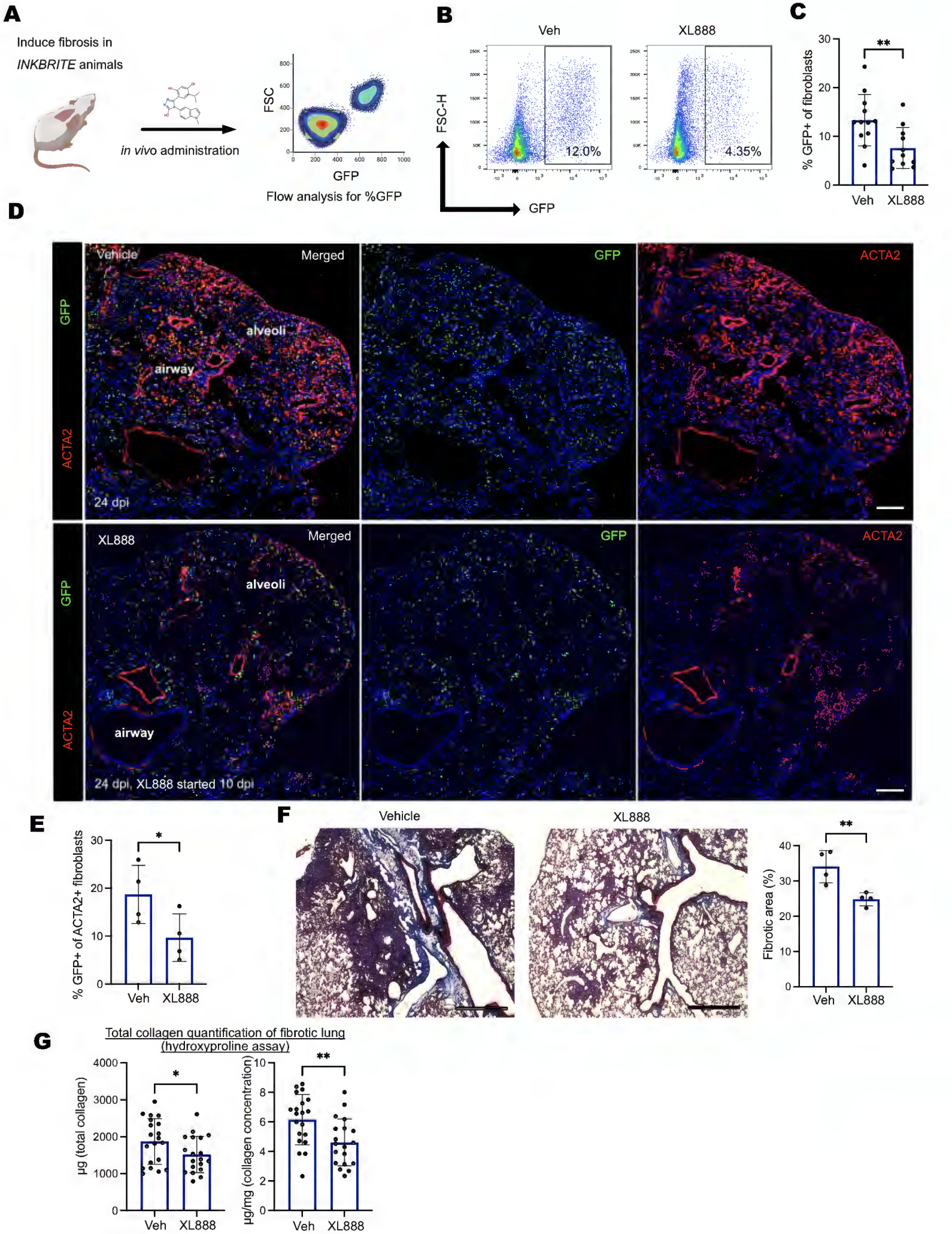
A
Induce fibrosis in
INKBRITE animals
in vivo administration
FSC
GFP
Flow analysis for %GFP
B
Veh
XL888
FSC-H
GFP
12.0%
4.35%
C
% GFP+ of fibroblasts
Veh
XL888
D
Vehicle
Merged
GFP
ACTA2
alveoli
airway
24 dpi
XL888
24 dpi, XL888 started 10 dpi
E
% GFP+ of ACTA2+ fibroblasts
F
Vehicle
XL888
Fibrotic area (%)
G
Total collagen quantification of fibrotic lung
(hydroxyproline assay)
µg (total collagen)
µg/mg (collagen concentration)

Figure 6. Human *p16^{INK4a}*+ fibroblasts contribute to pathologic fibroblasts in IPF.

(**A**) UMAP plot of fibroblast subsets seen in normal human and IPF lungs.

(**B**) Violin plot showing *CDKN2A* expression in the pathologic fibroblast cluster of IPF fibroblasts.

(**C**) Violin plots showing the profibrotic genes in the different fibroblast subsets.

(**D**) Visualization of *CDKN2A*, *CTHRC1*, *COL1A1*, and *ACTA2* expression patterns in human lung fibroblasts in IPF and control donor lungs.

(**E**) Representative images showing ACTA2+p16^{INK4a}+ pathologic fibroblasts (arrows) in lung sections of controls and subjects with IPF. Scale bars, 100 μm.

(**F**) qPCR analysis of genes enriched in pathologic fibroblasts in *p16^{INK4a}* high and low fibroblasts isolated from lungs of IPF patients (n = 9 technical replicates, experiments repeated with separate IPF donor fibroblasts at least 3 times).

Data are represented as mean ± SD.; **P* < 0.05; ***P* < 0.01; ****P* < 0.001; two-tailed Student's t test (**F**).

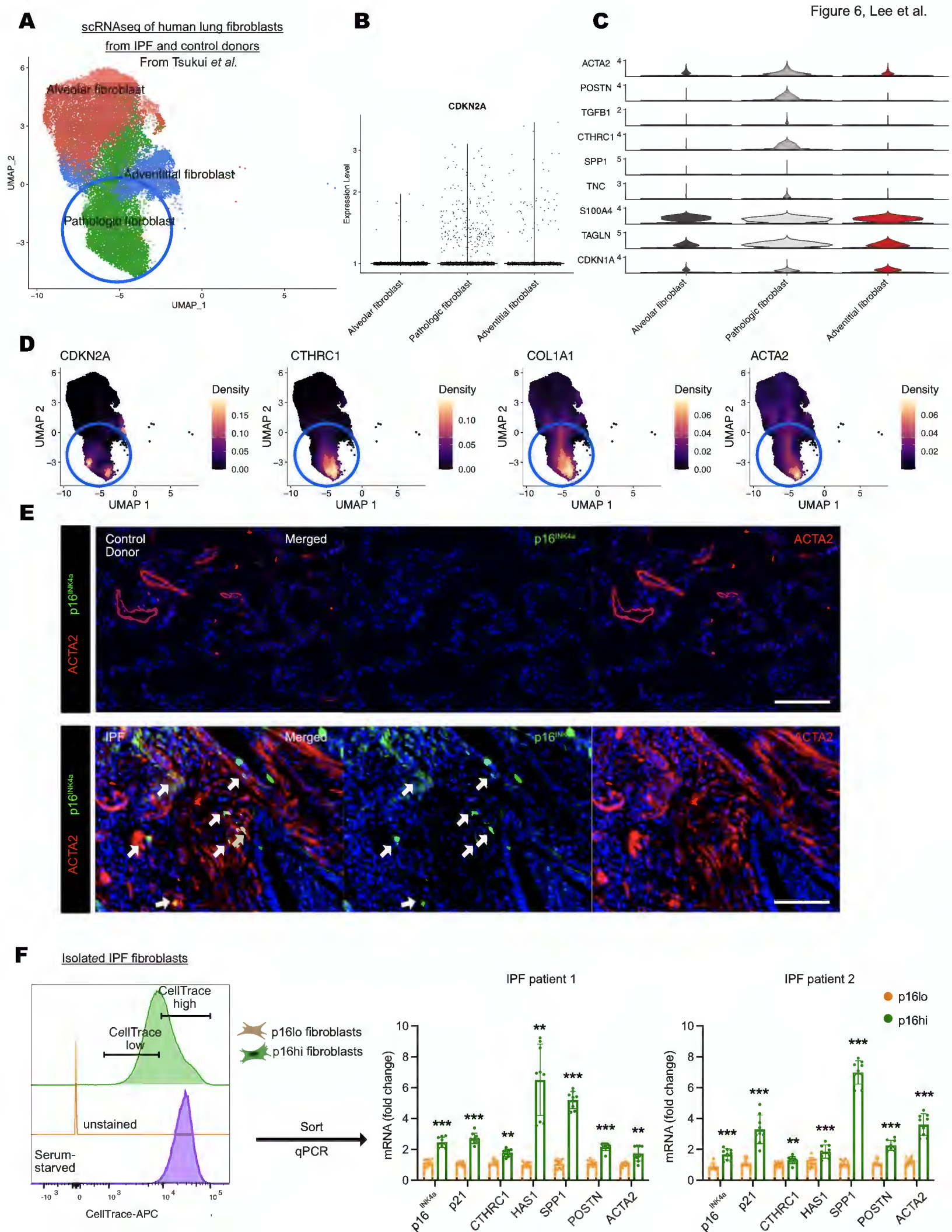
A
scRNAseq of human lung fibroblasts
from IPF and control donors
From Tsukui et al.
Alveolar fibroblast
Adventitial fibroblast
Pathologic fibroblast
UMAP_1
UMAP_2
B
CDKN2A
Expression Level
Alveolar fibroblast
Pathologic fibroblast
Adventitial fibroblast
C
ACTA2
POSTN
TGFB1
CTHRC1
SPP1
TNC
S100A4
TAGLN
CDKN1A
Alveolar fibroblast
Pathologic fibroblast
Adventitial fibroblast
D
CDKN2A
CTHRC1
COL1A1
ACTA2
Density
UMAP 1
UMAP 2
E
Control Donor
Merged
p16INK4a
ACTA2
IPF
F
Isolated IPF fibroblasts
CellTrace high
CellTrace low
unstained
Serum-starved
CellTrace-APC
p16lo fibroblasts
p16hi fibroblasts
Sort
qPCR
IPF patient 1
IPF patient 2
p16lo
p16hi
mRNA (fold change)
p16INK4a
p21
CTHRC1
HAS1
SPP1
POSTN
ACTA2

Figure 7. XL888 targets human *p16^{INK4a}*+ fibroblasts from IPF lungs *in vitro* and *ex vivo*.

(**A**) (Left) Schematic outline of dose-escalation challenge of candidate senolytics on *p16^{INK4a}* high and low fibroblasts isolated from IPF lungs (Right) Ratio of *p16^{INK4a}*-hi and *p16^{INK4a}*-lo fibroblast's cell count after treatment of senolytics and XL888 with dose-escalation (n = 3 technical replicates, experiments repeated with separate IPF donor fibroblasts at least 3 times).

(**B**) Schematic diagram depicting *ex vivo* culture of IPF lung with XL888 treatment and bright field images of cultured human PCLS. Scale bars, 2000 μm.

(**C**) Immunofluorescence analysis and quantification of ACTA2+ p16^{INK4a}+ cells in vehicle or XL888-treated hPCLS (n=12 slices per condition, sampled from 4 IPF donors independently, each color represents a different donor). Scale bars, 100 μm.

(**D**) Immunofluorescence analysis and quantification of CTHRC1+ p16^{INK4a}+ cells in vehicle or XL888-treated hPCLS (n=12 slices per condition, sampled from 4 IPF donors independently, each color represents a different donor). Scale bars, 100 μm.

Data are represented as mean ± SD.; *$P < 0.05$; **$P < 0.01$; ***$P < 0.001$; two-tailed Student's t test (**A**, **C**, **D**).

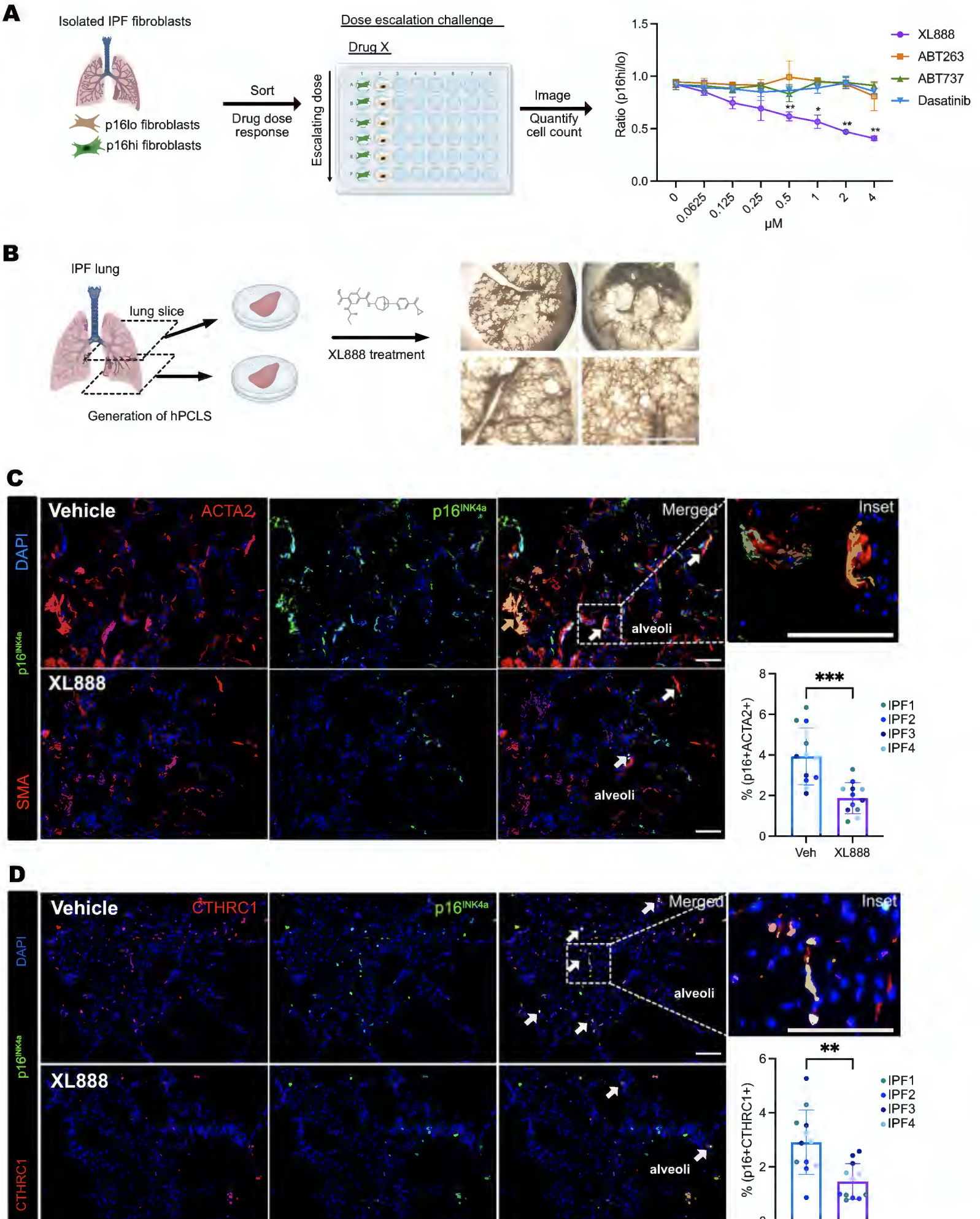
A
Isolated IPF fibroblasts
p16lo fibroblasts
p16hi fibroblasts
Sort
Drug dose response
Dose escalation challenge
Drug X
Escalating dose
Image
Quantify cell count
Ratio (p16hi/lo)
XL888
ABT263
ABT737
Dasatinib
μM
B
IPF lung
lung slice
Generation of hPCLS
XL888 treatment
C
Vehicle
ACTA2
p16INK4a
Merged
Inset
alveoli
XL888
DAPI
SMA
% (p16+ACTA2+)
IPF1
IPF2
IPF3
IPF4
Veh
XL888
D
Vehicle
CTHRC1
XL888
CTHRC1
% (p16+CTHRC1+)

References

1. Hayflick L, and Moorhead PS. The serial cultivation of human diploid cell strains. *Exp Cell Res.* 1961;25:585-621.
2. Gorgoulis V, Adams PD, Alimonti A, Bennett DC, Bischof O, Bishop C, et al. Cellular Senescence: Defining a Path Forward. *Cell.* 2019;179(4):813-27.
3. Burd CE, Sorrentino JA, Clark KS, Darr DB, Krishnamurthy J, Deal AM, et al. Monitoring tumorigenesis and senescence in vivo with a p16(INK4a)-luciferase model. *Cell.* 2013;152(1-2):340-51.
4. Baker DJ, Wijshake T, Tchkonia T, LeBrasseur NK, Childs BG, van de Sluis B, et al. Clearance of p16Ink4a-positive senescent cells delays ageing-associated disorders. *Nature.* 2011;479(7372):232-6.
5. Demaria M, Ohtani N, Youssef SA, Rodier F, Toussaint W, Mitchell JR, et al. An essential role for senescent cells in optimal wound healing through secretion of PDGF-AA. *Dev Cell.* 2014;31(6):722-33.
6. Baker DJ, Childs BG, Durik M, Wijers ME, Sieben CJ, Zhong J, et al. Naturally occurring p16(Ink4a)-positive cells shorten healthy lifespan. *Nature.* 2016;530(7589):184-9.
7. Chang J, Wang Y, Shao L, Laberge RM, Demaria M, Campisi J, et al. Clearance of senescent cells by ABT263 rejuvenates aged hematopoietic stem cells in mice. *Nat Med.* 2016;22(1):78-83.
8. Childs BG, Baker DJ, Wijshake T, Conover CA, Campisi J, and van Deursen JM. Senescent intimal foam cells are deleterious at all stages of atherosclerosis. *Science.* 2016;354(6311):472-7.
9. Demaria M, O'Leary MN, Chang J, Shao L, Liu S, Alimirah F, et al. Cellular Senescence Promotes Adverse Effects of Chemotherapy and Cancer Relapse. *Cancer Discov.* 2017;7(2):165-76.
10. Zhu Y, Tchkonia T, Pirtskhalava T, Gower AC, Ding H, Giorgadze N, et al. The Achilles' heel of senescent cells: from transcriptome to senolytic drugs. *Aging Cell.* 2015;14(4):644-58.
11. Ovadya Y, and Krizhanovsky V. Strategies targeting cellular senescence. *J Clin Invest.* 2018;128(4):1247-54.
12. Hernandez-Segura A, de Jong TV, Melov S, Guryev V, Campisi J, and Demaria M. Unmasking Transcriptional Heterogeneity in Senescent Cells. *Curr Biol.* 2017;27(17):2652-60 e4.
13. Wiley CD, Flynn JM, Morrissey C, Lebofsky R, Shuga J, Dong X, et al. Analysis of individual cells identifies cell-to-cell variability following induction of cellular senescence. *Aging Cell.* 2017;16(5):1043-50.
14. Reyes NS, Krasilnikov M, Allen NC, Lee JY, Hyams B, Zhou M, et al. Sentinel p16(INK4a+) cells in the basement membrane form a reparative niche in the lung. *Science.* 2022;378(6616):192-201.
15. Kirkland JL, and Tchkonia T. Senolytic drugs: from discovery to translation. *J Intern Med.* 2020;288(5):518-36.
16. Barnes PJ, Baker J, and Donnelly LE. Cellular Senescence as a Mechanism and Target in Chronic Lung Diseases. *Am J Respir Crit Care Med.* 2019;200(5):556-64.
17. Merkt W, Bueno M, Mora AL, and Lagares D. Senotherapeutics: Targeting senescence in idiopathic pulmonary fibrosis. *Semin Cell Dev Biol.* 2020;101:104-10.
18. Disayabutr S, Kim EK, Cha SI, Green G, Naikawadi RP, Jones KD, et al. miR-34 miRNAs Regulate Cellular Senescence in Type II Alveolar Epithelial Cells of Patients with Idiopathic Pulmonary Fibrosis. *PLoS One.* 2016;11(6):e0158367.

19. Habermann AC, Gutierrez AJ, Bui LT, Yahn SL, Winters NI, Calvi CL, et al. Single-cell RNA sequencing reveals profibrotic roles of distinct epithelial and mesenchymal lineages in pulmonary fibrosis. *Sci Adv.* 2020;6(28):eaba1972.
20. Adams TS, Schupp JC, Poli S, Ayaub EA, Neumark N, Ahangari F, et al. Single-cell RNA-seq reveals ectopic and aberrant lung-resident cell populations in idiopathic pulmonary fibrosis. *Sci Adv.* 2020;6(28):eaba1983.
21. Schafer MJ, White TA, Iijima K, Haak AJ, Ligresti G, Atkinson EJ, et al. Cellular senescence mediates fibrotic pulmonary disease. *Nat Commun.* 2017;8:14532.
22. Tsukui T, Sun KH, Wetter JB, Wilson-Kanamori JR, Hazelwood LA, Henderson NC, et al. Collagen-producing lung cell atlas identifies multiple subsets with distinct localization and relevance to fibrosis. *Nat Commun.* 2020;11(1):1920.
23. Tsukui TSD. Tracing the origin of pathologic pulmonary fibroblasts. *bioRxiv.* 2022;https://doi.org/10.1101/2022.11.18.517147.
24. Chaib S, Tchkonia T, and Kirkland JL. Cellular senescence and senolytics: the path to the clinic. *Nat Med.* 2022;28(8):1556-68.
25. Lehmann M, Korfei M, Mutze K, Klee S, Skronska-Wasek W, Alsafadi HN, et al. Senolytic drugs target alveolar epithelial cell function and attenuate experimental lung fibrosis ex vivo. *Eur Respir J.* 2017;50(2).
26. Blokland KEC, Waters DW, Schuliga M, Read J, Pouwels SD, Grainge CL, et al. Senescence of IPF Lung Fibroblasts Disrupt Alveolar Epithelial Cell Proliferation and Promote Migration in Wound Healing. *Pharmaceutics.* 2020;12(4).
27. Blay V, Tolani B, Ho SP, and Arkin MR. High-Throughput Screening: today's biochemical and cell-based approaches. *Drug Discov Today.* 2020;25(10):1807-21.
28. Zhu Y, Tchkonia T, Fuhrmann-Stroissnigg H, Dai HM, Ling YY, Stout MB, et al. Identification of a novel senolytic agent, navitoclax, targeting the Bcl-2 family of anti-apoptotic factors. *Aging Cell.* 2016;15(3):428-35.
29. Fuhrmann-Stroissnigg H, Ling YY, Zhao J, McGowan SJ, Zhu Y, Brooks RW, et al. Identification of HSP90 inhibitors as a novel class of senolytics. *Nat Commun.* 2017;8(1):422.
30. Lomas NJ, Watts KL, Akram KM, Forsyth NR, and Spiteri MA. Idiopathic pulmonary fibrosis: immunohistochemical analysis provides fresh insights into lung tissue remodelling with implications for novel prognostic markers. *Int J Clin Exp Pathol.* 2012;5(1):58-71.
31. Cohn RL, Gasek NS, Kuchel GA, and Xu M. The heterogeneity of cellular senescence: insights at the single-cell level. *Trends Cell Biol.* 2023;33(1):9-17.
32. Nichelle I. Winters CJT, Christopher S. Jetter, Jane E. Camarata, Austin J. Gutierrez, Linh T. Bui, Jason J. Gokey, Matthew Bacchetta, Nicholas E. Banovich, Jennifer M.S. Sucre, Jonathan A. Kropski. Single-cell transcriptomic assessment of cellular phenotype stability in human precision-cut lung slices. *bioRxiv.* 2021.
33. Magyar CTJ, Vashist YK, Stroka D, Kim-Fuchs C, Berger MD, and Banz VM. Heat shock protein 90 (HSP90) inhibitors in gastrointestinal cancer: where do we currently stand?-A systematic review. *J Cancer Res Clin Oncol.* 2023;149(10):8039-50.